Hetero-oligomer Nanoparticle Arrays for Plasmon-Enhanced Hydrogen Sensing

Ankun Yang,[†] Mark D. Huntington,[†] M. Fernanda Cardinal,[‡] Sicelo S. Masango,[‡] Richard P. Van Duyne,[‡] and Teri W. Odom[†,‡,*]

[†]Department of Materials Science & Engineering and [‡]Department of Chemistry, Northwestern University, Evanston, Illinois 60208, United States

ABSTRACT This paper describes how the ability to tune each nanoparticle in a plasmonic hetero-oligomer can optimize architectures for plasmon-enhanced applications. We demonstrate how a large-area nanofabrication approach, reconstructable mask lithography (RML), can achieve independent control over the size, position, and material of up to four nanoparticles within a subwavelength unit. We show how arrays of plasmonic hetero-oligomers consisting of strong plasmonic materials (Au) and reactant-specific elements (Pd) provide a unique platform for enhanced hydrogen gas sensing. Using finite-difference time-domain simulations, we modeled different configurations of Au–Pd hetero-oligomers and compared their hydrogen gas sensing capabilities. In agreement with calculations, we found that Au–Pd nanoparticle dimers showed a red-shift and that Au–Pd trimers with touching Au and Pd nanoparticles showed a blue-shift upon exposure to both high and low concentrations of hydrogen gas. Both Au–Pd hetero-oligomer sensors displayed high sensitivity, fast response times, and excellent recovery.

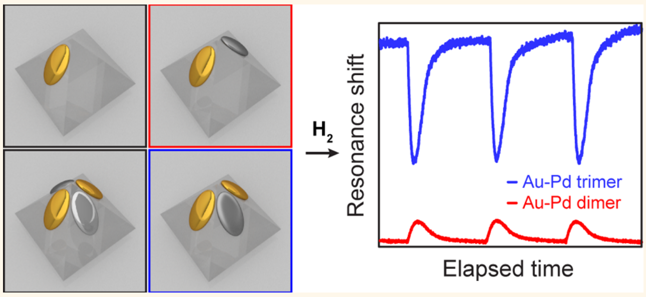

KEYWORDS: plasmonic assemblies · heterogeneous oligomers · nanofabrication · hydrogen sensing · Au–Pd nanoparticle dimers · Au–Pd nanoparticle trimers

Metallic nanoparticles (NPs) can spatially confine light on the nanometer scale by trapping energy into localized surface plasmon (LSP) modes.[1–3] The LSP resonance of a single NP depends on the material, size, and shape as well as the local dielectric environment.[4] This localized mode can also be tuned by placing another metal NP in close proximity (<50 nm),[5] where the LSP of one particle can couple to the other through dipolar interactions.[6] Furthermore, plasmonic NPs arranged into assemblies (three or more NPs) can manipulate near-field profiles[7–9] and modify far-field characteristics compared to a single NP.[8] For example, Au NP trimers can enhance the intensity of dark plasmon modes,[8,10] and Au NP tetramers can preserve the polarization state of incident light while enhancing the local field.[11] The intense localized fields confined within the gaps of NP assemblies have been exploited for applications such as surface-enhanced Raman scattering[12] and plasmon-enhanced biological and chemical sensing.[13] Plasmonic assemblies made from different materials (*e.g.*, Au–Ag NP dimers) can show otherwise forbidden optical signatures because of composition asymmetry.[14,15] Plasmonic heteroparticle assemblies can also boost the function of weak or nonplasmonic materials in plasmon-enhanced chemistries.[16,17] For example, Au–Pd NP dimers and Au@Pd core–shell nanocrystals have been tested as H_2 gas sensors[16,18] because Pd NPs can rapidly incorporate hydrogen gas due to short diffusion lengths for H atoms, while the enhanced near-fields of Au NPs sensitively detect and report changes in Pd NPs as far-field spectral shifts.

Bottom-up methods that can organize metallic NPs into well-defined assemblies typically involve molecular linkers with specific recognition properties. For example, the hybridization of complementary DNA strands can facilitate the assembly of Au NPs into extended structures[19] with control over NP separation down to 0.5 nm;[20] however,

* Address correspondence to todom@northwestern.edu.

Received for review May 7, 2014 and accepted June 23, 2014.

10.1021/nn502502r

these and other solution approaches have low NP assembly yield and require substantial purification processes.[9,14,20−24] The most common top-down approach to design plasmonic NP assemblies, including dimers,[5,12] tetramers,[7] and heptamers,[25] is electron beam lithography (EBL). EBL can produce nanostructures with more than one material in a subwavelength region but requires both high alignment accuracy and precision between metal depositions.[16] EBL also has limited throughput. Template-assisted lithography is a promising parallel strategy for inexpensive fabrication of plasmonic NP assemblies[26] but has only realized arrays of simple geometries[27−31] and/or two materials[15,17] because of the prefixed masks involved in the procedures. Therefore, the fabrication of plasmonic heterogeneous NP assemblies with high throughput remains a fundamental challenge.

Here we present a nanofabrication approach—reconstructable mask lithography (RML)—that can create large-area arrays of plasmonic hetero-oligomers within a subwavelength footprint. Access to well-defined assemblies of plasmonic NPs can facilitate the emergence of new design principles to optimize plasmon-enhanced applications. First, we built up Au NP oligomers from a monomer unit to a tetramer assembly. The construction of NP trimers and tetramers resulted in the formation of side gaps besides a center gap, which modulated the properties of these higher ordered assemblies. Next, we examined the versatility of RML by designing plasmonic hetero-oligomers consisting of both strong plasmonic materials (Au) and reactant-specific elements (Pt and Pd). We used Au−Pd NP dimer and trimer assemblies to study the coupling between Pd and two different Au nanoantennas for hydrogen sensing. We found that Au−Pd dimers showed small red-shifts while Au−Pd trimers showed large blue-shifts upon hydrogen injection depending on the size of the side gap. Centimeter-scale substrates of both types of Au−Pd hetero-oligomers showed fast response times (seconds) and recovery without hysteresis.

RESULTS AND DISCUSSION

Figure 1 depicts the parallel fabrication scheme of RML to create plasmonic oligomer arrays over large areas. First, a square array of nanoholes (d = 200 nm, a_0 = 400 nm) in a Ti film was patterned on Si(100) wafers by a combination of phase-shifting photolithography[32,33] to define posts in the photoresist (Methods), deposition of a thin Ti layer (10 nm), and lift-off. We used an anisotropic KOH etch to create pyramidal Si pits beneath the circular Ti holes; the pits provided the subwavelength template to build the plasmonic oligomers. The substrates were mounted onto a rotational stage with an angle ψ relative to the e-beam deposition direction (ψ = 0°, normal to the surface; ψ = 90°, parallel to surface).

A Cr slit mask was built on top of the Ti hole mask by Cr deposition at a high angle ψ_{Cr} at two different in-plane azimuthal angles φ^1_{Cr} and φ^2_{Cr}. After the slit mask was constructed, plasmonic NPs with widths defined by the Cr slit could then be formed in the Si pit in subsequent plasmonic material depositions. For simplicity, we illustrate this process using Au as the plasmonic metal. Au can be deposited at a relatively low angle ψ_{Au} at azimuthal angles φ^1_{Au} and φ^2_{Au} (or only φ^1_{Au}) to produce Au dimers (monomers). The production of a Cr slit mask above the circular Ti hole array

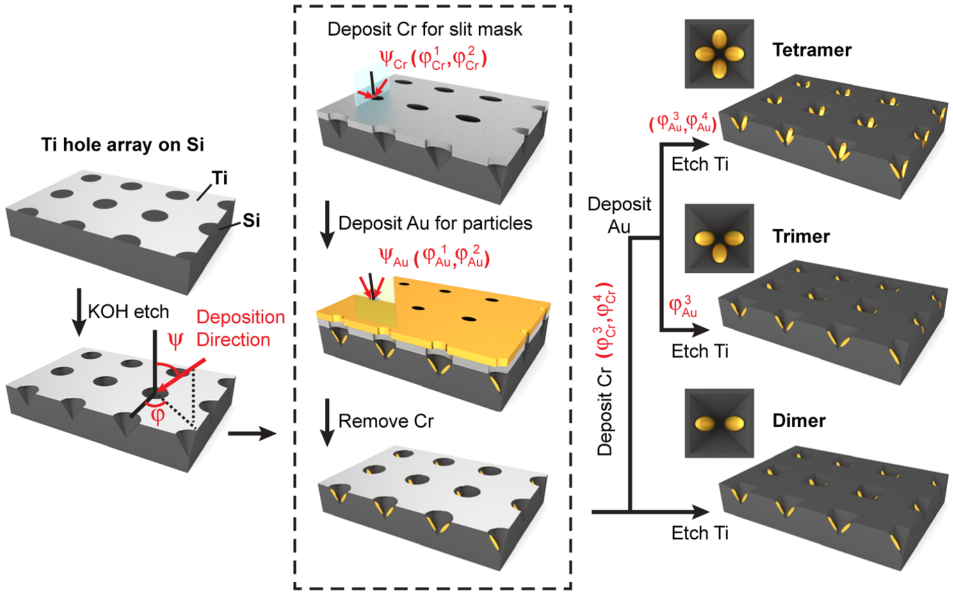

Figure 1. Scheme of reconstructable mask lithography. Deposition angles in 3D model are ψ_{Cr} = 50° to create the Cr slit mask and ψ_{Au} = 20° to create the NPs. The azimuthal angles are φ^1_{Cr} = 0°, φ^2_{Cr} = 180°, φ^3_{Cr} = 90°, φ^4_{Cr} = 270°; φ^1_{Au} = 90°, φ^2_{Au} = 270°, φ^3_{Au} = 0°, φ^4_{Au} = 180°.

constitutes the most important step in RML because this top Cr mask can be removed and reconstructed between sequential depositions of the desired plasmonic materials *without* the need to change the underlying Ti hole array. The reconstructable Cr mask, together with the deposition angle ψ_{Au}, determines the size, shape, and position of NPs within the Si template and allows the aspect ratio of the NPs as well as the center gap distance in a dimer to be tuned.

One distinct advantage of RML is that circular Ti holes can effectively become elliptical, which ensures that multiple NPs deposited into a subwavelength area can remain separated with defined gaps. We fabricated more than two NPs in one pit by repeating the process of Cr mask construction and plasmonic particle deposition. After two Au depositions to produce a dimer, the Cr film with slit holes was etched to reveal the underlying Ti circular hole arrays. Since Cr was deposited at high angles (50°), deposition of Cr onto the sidewalls of the pits was limited to the very top regions. There was only minimal overlap between deposited Au and Cr materials since Au was deposited at much lower angles (20°) and at perpendicular directions; therefore the Au NPs stayed in the Si pits after the Cr layer was etched.

Then, Cr was deposited at azimuthal angles φ^3_{Cr} and φ^4_{Cr} (the substrate was rotated 90°) to construct a second Cr slit mask. A third deposition of Au with deposition angle ψ_{Au} at φ^3_{Au} can result in a trimer, while the fourth deposition at φ^4_{Au} results in a tetramer. The configurability of Cr slit masks enables fabrication of more than two NPs with equal sizes in close proximity (10–20 nm), which is challenging for other parallel nanofabrication methods. Because each NP requires a separate deposition step, RML can achieve exquisite structural control over the size, position, and material of NPs in an assembly.

Using RML, we fabricated Au monomer, dimer, trimer, and tetramer NP arrays (Figure 2). The dimensions of the Cr slit mask and the deposition angle ψ_{Au} controlled the size of the particles, where we used a Cr slit mask with dimensions 130 nm × 70 nm and Au deposition at $\psi_{\mathrm{Au}} = 20°$ (30 nm) to result in a monomer NP with dimensions 120 nm × 60 nm × 30 nm (length × width × thickness, Figure 2a). The roughness of the Au NPs was related to the deposition conditions, including the vacuum and deposition rate. Patterns on the poly(dimethylsiloxane) stamp used in phase-shifting photolithography controlled spacings between adjacent NP oligomers (Supporting Information, Figure S1a). The aspect ratio of the Cr slit mask (length to width) defined the aspect ratio of the plasmonic Au NPs (Supporting Information, Figure S1b–e). The deposition angle ψ_{Au} effectively controlled the distance between the ends of the two NPs in the dimer (Figure 2b). Small gaps, on the order of a few nanometers, are desirable for many applications and can be realized by simply decreasing the deposition angle ψ_{Au} (Supporting Information, Figure S1f,g). Figure 2 shows results where the Cr slit mask was built along the high-symmetry directions of the square lattice, but RML can also produce NPs oriented along different directions (Supporting Information, Figure S1h,i).

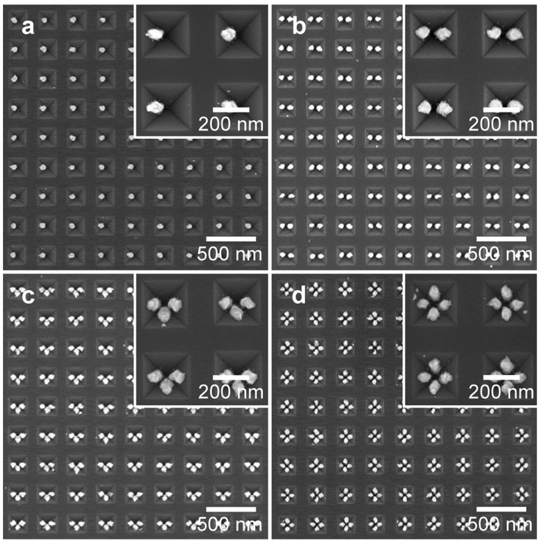

Figure 2. Au plasmonic oligomers. SEM images of arrays of (a) monomer, (b) dimer, (c) trimer, and (d) tetramer NPs. The insets show the structures at high magnification.

To produce Au NP assemblies with equal NP sizes, we kept the dimensions of the Cr slit mask (130 nm × 70 nm) and parameters for Au depositions ($\psi_{\mathrm{Au}} = 20°$, thickness = 30 nm) the same for NP trimers and tetramers. Trimers had two side gaps created by the third deposition of Au (Figure 2c), where the side gaps (10–20 nm) between neighboring particles were smaller than the center gap (30–40 nm) when the same deposition angle was used (20°). Tetramer NPs were formed by a fourth deposition of Au, which resulted in two more side gaps and a symmetric structure (Figure 2d). All plasmonic oligomers were 3D in shape because of the etched Si pyramidal pit. However, since RML can also be used with different Cr masks and substrates, 2D plasmonic oligomers can also be created (Supporting Information, Figure S2).

To investigate the optical properties of the plasmonic oligomers, we transferred the arrays from the Si templates onto transparent substrates *via* template stripping[34] using a UV-curable polymer (polyurethane, PU, NOA 61, Norland Products).[35] After template stripping, the oligomers were situated on a PU pyramid; the separation between nearest neighbor NPs within the subwavelength footprint was often reduced slightly (~5–10 nm) compared to that in the Si pit from PU shrinkage during the UV curing process. The transmission spectra were collected by a UV–vis spectrometer (Methods). To elucidate the plasmon modes of coupled modes in the oligomer NPs, we kept the polarization of light fixed where the electric field E was along the x-axis and across the center gap (Figure 3). Under this

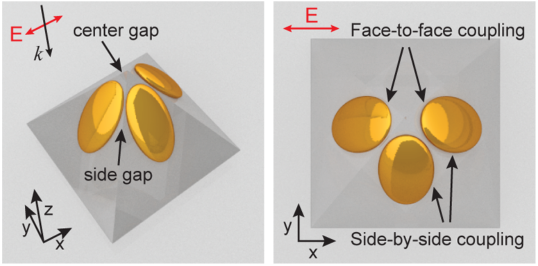

Figure 3. Scheme defining side gaps and center gap for Au NP trimers on a PU pyramid.

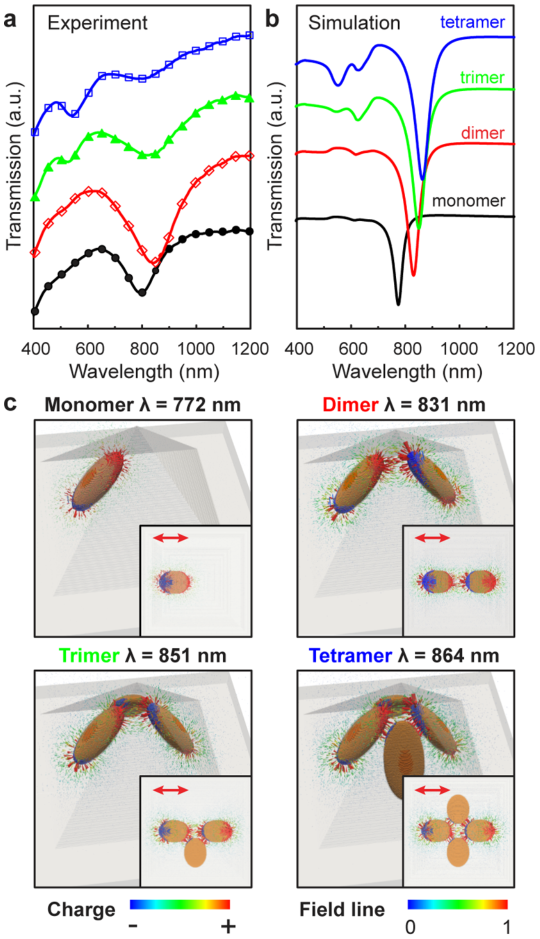

Figure 4. Optical properties of Au plasmonic oligomers. (a) Measured and (b) simulated transmission spectra of Au plasmonic oligomers. (c) Near-field optical profiles of the structures on resonance. The red arrows denote the polarization direction.

polarization, in a Au NP trimer, the two NPs separated by a center gap will have face-to-face plasmonic coupling, and they can also couple to the third NP in a side-by-side manner.

Plasmon hybridization is a useful phenomenological model that can explain the LSP resonance wavelengths of coupled structures in terms of the energies of isolated structures.[36] In this model, Au NP dimers support bonding (bright) and antibonding (dark) modes, where the bright mode should be red-shifted compared to a single NP.[37] Indeed, both measurement and simulation showed a clear red-shift from monomer to NP dimers (Figure 4a,b). From dimers to NP tetramers, the simulated spectra also showed small (<20 nm) red-shifts (Figure 4b). These wavelength shifts were not observed in experiment (Figure 4a); we attribute this mismatch to plasmonic damping effects from surface roughness and averaging from large sample areas (~1 cm^2).

The monomer exhibited a dipolar mode (λ = 772 nm), where the charges were separated at two ends, and electric field lines circulated around the NP (Figure 4c). In the dimer, coupling of the two NPs resulted in charge redistribution and a resonance split. The antibonding mode was dark since there was no net dipole moment; the bonding mode with opposite charges across the gap showed up at a longer wavelength (λ = 831 nm), causing a red-shift in resonance from monomer to dimer. Because the coupling between two NPs in a dimer was in a face-to-face configuration, the red-shift was large ($\Delta\lambda$ = 59 nm). The optical field was concentrated and enhanced in the center gap (Supporting Information, Figure S3a). Enlarged 2D projection views of the insets can be found in the Supporting Information (Figure S4). Since Au dimer arrays have C_{2v} symmetry, the dimers exhibited a polarization-dependent response (Supporting Information, Figure S5).

In our 3D NP oligomers, trimers were especially interesting because two side gaps were formed as a vertical particle (2D projection view, Figure 4c inset) was added to the dimer. This vertical particle bridged part of the electric field lines and produced another coupling channel for the two horizontal particles (Figure 4c). Notably, the charges had opposite signs across side gaps, which decreased the restoring force acting on the oscillating electrons of the NP dimer and thus resulted in a red-shift of the resonance compared to that of the dimer (λ = 851 nm, $\Delta\lambda$ = 20 nm). The optical fields were strongly confined within the side gaps for trimers (Supporting Information, Figure S3b). Because coupling between the two horizontal particles and the vertical particle was from side-by-side interactions, the overall red-shift ($\Delta\lambda$ = 20 nm) was smaller than that from monomer to dimer ($\Delta\lambda$ = 59 nm). Analogously, the tetramer was composed of a trimer and another vertical particle, which further red-shifted the resonance (λ = 864 nm, $\Delta\lambda$ = 13 nm). Au tetramer arrays have C_{4v} symmetry and show a polarization-independent response (Supporting Information, Figure S5).

Experiment was unable to resolve the high-energy modes of trimers and tetramers and showed only one resonance envelope (Figure 4a). The high-energy modes around 550 nm were dominated by transverse modes supported by the vertical NPs and also showed complex charge distributions (Supporting Information, Figure S3c). Compared to simulations, the experimental

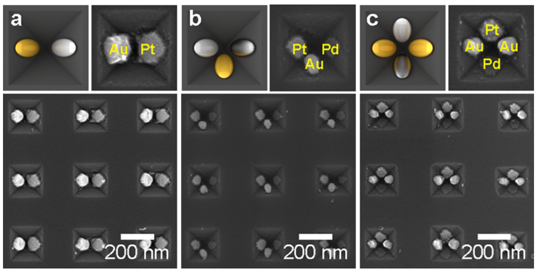

Figure 5. Hetero-oligomers with tunable material for each single particle. SEM images of (a) Au−Pt heterodimers, (b) Au−Pd−Pt heterotrimers, and (c) Au−Pd−Pt hetero-tetramers.

resonances were broader, which can possibly be attributed to small size variations in the NPs across the large-area substrates (~1 cm^2). To assess the effects of structural inhomogeneity on the LSP resonances, we analyzed SEM images and obtained oligomer NP size statistics (Supporting Information, Table S1). We calculated the LSP resonances of tetramers using different NP sizes (Supporting Information, Figure S6). Compared to simulations based on a single NP size, the LSP resonance of the tetramer NP weighted by the size distribution could be broadened by up to 50 nm while the resonance position shifted within $\Delta\lambda$ = 15 nm.

One distinct advantage of RML over other template-assisted methods is the ability to control the composition of each NP in the subwavelength unit. A collection of plasmonic hetero-oligomers is accessible because we can replace the Au depositions with other plasmonic metals, and notably, these NPs could be deposited in any order. We chose Au antennas and materials that are commonly used in catalysis and sensing (Pt and Pd) to illustrate multimaterial arrays (Figure 5). To produce Au−Pt dimers, Au and Pt were deposited with $\psi = 20°$ at azimuthal angles $\varphi^1 = 90°$ and $\varphi^2 = 270°$ through a Cr slit mask. To demonstrate that RML can control the aspect ratio of NPs, we used a Cr slit mask with a width of 100 nm to obtain wide Au and Pt NPs (*ca.* 80 nm) (Figure 5a). Importantly, the two different metal depositions to produce NPs using the same Cr slit mask can be performed by rotating the substrate 180°. To construct Au−Pd−Pt trimers, we deposited Pt and Pd at azimuthal angles $\varphi^1 = 90°$ and $\varphi^2 = 270°$ using the first Cr slit mask built with angles $\varphi^1_{Cr} = 0°$ and $\varphi^2_{Cr} = 180°$. Then, we constructed the second Cr slit mask using azimuthal angles $\varphi^1_{Cr} = 90°$ and $\varphi^2_{Cr} = 270°$ and deposited Au at azimuthal angle $\varphi^3 = 90°$ (Figure 5b). Following similar procedures, we added another Au NP and created Au−Pd−Pt tetramers with two Au nanoantennas (Figure 5c). Arrays of plasmonic hetero-oligomers can be fabricated over large areas with high uniformity (Supporting Information, Figure S7). The assembly of NPs with different compositions is a step toward integration of multifunctions within deep subwavelength footprints.

The design of H_2 sensors has received increasing interest because of the expanded use of H_2 as a chemical reactant and as an energy carrier.[16,17,38] H_2 needs to be detected at low concentrations (0.01−10%) for safety applications and over a wide range (1−100%) for monitoring processes in the fuel cell industry.[39] Our hetero-oligomers provide a unique platform where Au and Pd NPs can be organized into multiple configurations to test and compare their H_2 detection performances. We first analyzed the performance of different Au−Pd NP oligomers using finite-difference time-domain (FDTD) simulations (Methods). We created Au nanoantennas from a single Au NP or a Au NP dimer and then situated the Pd NP to form either Au−Pd dimers or Au−Pd trimers. In these architectures, the optical near-fields are primarily enhanced within the center gap or two side gaps, respectively (Supporting Information, Figure S3). We investigated the change in far-field spectra and near-field profiles of the Au−Pd oligomers before and after H_2 injection.

In the simulations, we considered two competing factors when H_2 adsorbed to Pd: dielectric change and lattice expansion.[40] The dielectric function of Pd is modified when electrons from H enter the s- and d-bands of Pd and change the density of states at the Fermi level.[41,42] Pd becomes less metallic after absorption of H_2.[42] Meanwhile, dissociated hydrogen atoms (H) in Pd form a solid solution (α-phase) at low concentrations (H/Pd ≈ 0.015) but palladium hydride (PdH_x, β-phase) at high concentrations (H/Pd ≈ 0.6). The β-phase is less mobile than the α-phase and can result in a pronounced lattice expansion, as much as 4% (at room temperature, a_0 changes from 0.3894 to 0.4040 nm).[40,43] For simplicity, we assumed a complete conversion of Pd into PdH_x and used a 4% lattice expansion. The dimensions of Au and Pd NPs were set close to experiment (120 nm × 60 nm × 30 nm). To elucidate separate effects of dielectric change and lattice expansion, we performed three simulations to compare the resonances with that of Au−Pd oligomers without hydrogen injection. In the first simulation, we considered only the dielectric change by replacing Pd with PdH_x. In the second, we only expanded the Pd NP by multiplying the dimensions with a scaling factor 1.04. In the third, we expanded the size of the Pd NP and then changed its dielectric function to represent PdH_x. In a Au−Pd dimer, the dielectric change of Pd resulted in a blue-shift ($\Delta\lambda$ = 16 nm) because the refractive index of the Pd NP decreased after H_2 absorption.[44] Lattice expansion in Pd produced a larger red-shift ($\Delta\lambda$ = 18 nm) because the increased size of the Pd/PdH_x NP reduced the gap distance. When both effects were considered, the overall effect was a red-shift of 6 nm (Figure 6a). Although the net wavelength shift can be understood based on the two separate effects, their effects cannot be combined linearly. The dielectric change and lattice expansion in Pd affected the near-field response of the Au NP ($|E|^2/|E_0|^2$ dropped

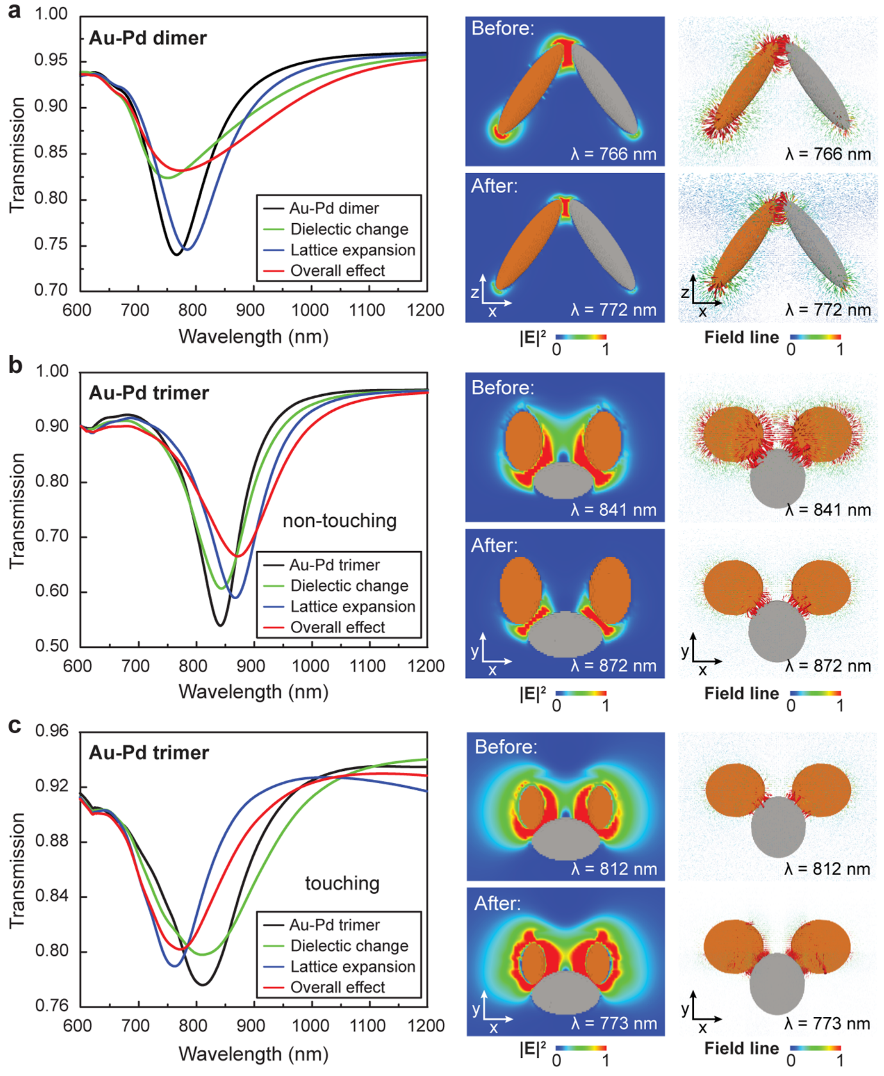

Figure 6. FDTD simulations for Au–Pd dimers and trimers upon hydrogen injection. Far-field spectral shifts and near-field profiles of electric field enhancement and charge distribution for (a) Au–Pd dimers, (b) Au–Pd trimers (nontouching), and (c) Au–Pd trimers (touching). For near-field profiles of Au–Pd dimers, *x*–*z* cross sections are shown. For Au–Pd trimers, *x*–*y* cross sections of the smallest side gaps are shown for $|E|^2$ and top-down projections for field lines. In all the simulations, light was polarized along the *x*-axis.

from 9 × 10^2 to 3 × 10^2) and caused a far-field spectral shift compared to that before hydrogen injection.

Since Au–Pd trimers support very small side gaps, Au and Pd NPs have the potential to touch. Therefore, we performed a series of simulations where the side gap was gradually reduced to zero to understand this gap effect on the LSP resonance (Supporting Information, Figure S8a). Under polarization parallel to the Au NP dimer axis, Au–Pd trimers supported one resonance (between 700 and 900 nm) when there were side gaps and two resonances when Au and Pd NPs touched (one between 700 and 900 nm and the other at *ca*. 1500 nm, not shown). For each side-gap separation, we included effects from hydrogen incorporation based on Pd dielectric change and lattice expansion and found that the overall resonance shift direction depended on whether the Au and Pd NPs were touching or not (Supporting Information, Figure S8b).

When Au and Pd NPs were separated before H_2 injection (side-gap >0 nm), the resonance red-shifted upon H_2 injection. This red-shift decreased exponentially as the side gap increased, which indicated weaker influence of the change in Pd on the resonance when the Pd NP moved away from the Au dimer. As a specific example, we investigated a side gap of 4 nm (Figure 6b) and found that the dielectric function change mainly broadened the resonance; the lattice expansion dominated in this small-gap regime and resulted in a red-shift of the resonance. The field enhancement in the gaps did not change ($|E|^2/|E_0|^2$: 3 × 10^3), although more energy was confined within the side gaps. Interestingly, if the side-gap separation was zero, and Au and Pd NPs touched before H_2 injection, the resonance blue-shifted after H_2 injection (Figure 6c). In this case, the Au and Pd NPs formed a narrow conducting link that could induce anomalously

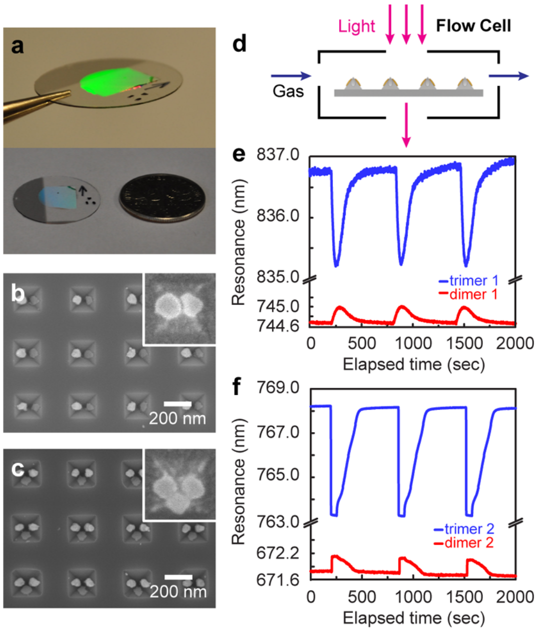

Figure 7. Au–Pd dimer and trimer arrays as hydrogen gas sensors. (a) Photographs of Au–Pd trimer on a glass coverslip. A U.S. dime is shown for comparison. Representative SEM images of Au–Pd (b) dimers and (c) trimers in Si pits. Insets show structures in PU after template stripping. (d) Scheme of the measurement setup. Responses of Au–Pd dimer and trimer arrays upon injection of 100% H_2 are shown in red and blue. (e) Injection with 5 s of 8 sccm H_2 and then 10 min of 25 sccm N_2 (three cycles). (f) Injection with 60 s of 50 sccm H_2 and then 10 min of 100 sccm N_2 (three cycles).

large field enhancement at the contacting surfaces.[5] The expanded Pd lattice resulted in more energy confinement between Au and Pd NPs ($|E|^2/|E_0|^2$ increased from 2×10^3 to 6×10^3) (Figure 6c), and since the dielectric constant of PdH_x is lower than Pd, the resonance was blue-shifted.

According to simulations, the change in the Pd NP upon H_2 injection could modify the near-field profiles of Au NPs, and conversely, the enhanced optical fields of Au NPs sensitively detected and reported the changes in the Pd NP as observable far-field spectral shifts. Therefore, we aimed to design Au–Pd oligomers with very small gaps between the Au and Pd NPs since the structural change of Pd had a dominating effect in the small-gap size regime (<10 nm). We fabricated Au–Pd dimer and trimer arrays using RML and compared their H_2 sensing performance. The large-area arrays were uniform across the sample (Figure 7a) and had very small center gaps (<25 nm in Si; <15 nm in PU) and side gaps (<20 nm in Si; <10 nm in PU) (Figure 7b,c). The samples were placed in a gas flow cell (Figure 7d), and extinction spectra were collected by high-resolution localized surface plasmon resonance (HR-LSPR) spectroscopy (resolution: 0.015 nm, Methods).[13,45] N_2 was used to purge the system, and then H_2 was injected with different flow rates to study the response of the system under different doses of H_2. The extinction spectra of Au–Pd oligomers under unpolarized light showed two resonances in the visible and near-infrared wavelength range (Supporting Information, Figure S9). For sensing, we monitored both resonances but found only the resonance involved in coupling between Pd and Au NPs (650–850 nm) showed H_2-sensing behavior.

With an injection of 8 sccm 100% H_2 for 5 s, a red-shift ($\Delta\lambda = 0.3$ nm) of the resonance was observed in Au–Pd dimer arrays, while a blue-shift ($\Delta\lambda = 1.5$ nm) was observed in Au–Pd trimer arrays (Figure 7e). The NP response time was fast (seconds) and reproducible, and the maximum responses (largest spectral shifts) occurred approximately 1 min after H_2 injection. We also tested another set of samples with higher flow rates and longer injection times. With a 60 s injection of 50 sccm 100% H_2, both Au–Pd dimers and trimers showed larger spectral shifts ($\Delta\lambda = 0.4$ nm and $\Delta\lambda = 5$ nm, Figure 7f). In the latter case, we observed that the maximum responses occurred ~10 s after H_2 injection, which were faster than those under low flow rates. A clear saturation plateau indicated that the incorporation of H into the Pd lattice reached equilibrium (Figure 7f). The magnitude of the LSP resonance shift was reproducible over at least 10 cycles (Supporting Information, Figure S10). To examine the long-term stability of these substrates, we retested these oligomer NP sensors two months after the first set of experiments and observed reproducible shifts very similar to that of the original ones (Supporting Information, Figure S11).

The red-shifts observed in the Au–Pd dimer arrays agreed with simulation (Figure 6a), and the unexpected blue-shifts in the Au–Pd trimer arrays also matched the simulation results when Au and Pd NPs touched (Figure 6c). This scenario is plausible since small side gaps in Au–Pd trimers were observed in experiment (Figure 7c, inset), and during template stripping, curing of PU may cause shrinkage and closing of the side gaps. The H_2 pressure in the flow cell was >1000 mbar at room temperature, which, under equilibrium conditions, should achieve nearly 100% β-phase formation.[46] However, the resonance shifts in experiments were generally smaller than those in simulations, most likely because we used the largest lattice expansion value (4%). Moreover, since our NPs were partly embedded in PU, they may absorb less H_2 than assumed in simulations. A common drawback in Pd-based systems for H_2 detection is hysteresis[16–18] from lattice strain due to H incorporation and the residual H left in the Pd lattice. Significantly, almost no obvious hysteresis was observed in our Au–Pd dimer and trimer systems (Figure 7e,f), and the spectral shift was reproducible over many cycles tested. The absence or minimum of hysteresis as well as the fast response times demonstrates the promise of Au–Pd oligomer arrays for practical use in H_2 sensing.

We further investigated detection limits at much lower H_2 concentrations by cycling 2% H_2. The direction of the resonance shifts was consistent for both the Au−Pd dimers and trimers (NPs touching), but the magnitudes of the shifts were smaller (Supporting Information, Figure S12). With injection of 100 sccm 2% H_2 for 60 s, Au−Pd dimers showed a red-shift ($\Delta\lambda$ = 0.35 nm) and Au−Pd trimers showed a blue-shift ($\Delta\lambda$ = 0.7 nm). On the basis of these results at high (100%) and low (2%) concentrations, we expect plasmonic hetero-oligomers to be able to detect a wide range of H_2 concentrations after design optimization, which promises applications for both safety and fuel cell industry. We will first use FDTD simulations to optimize the sensor structures for concentration-dependent studies and then fabricate them using RML.

CONCLUSIONS

In summary, we report how arrays of hetero-oligomer NPs can be used for plasmon-enhanced gas sensing. We developed reconstructable mask lithography as an effective approach to produce large-area, uniform arrays of plasmonic homo-oligomer and hetero-oligomer units composed of as many as four NPs. We demonstrated that the optical properties of plasmonic oligomers could be tuned by controlling the size, relative position, and number of particles in each NP assembly. A detailed analysis on both simulations and experiments on Au−Pd hetero-oligomers was performed and correlated. Using FDTD simulations, we showed that upon hydrogen injection, Au−Pd dimers exhibited red-shifts and that Au−Pd trimers exhibited red-shifts or blue-shifts depending on whether the Au and Pd NPs touched. We experimentally confirmed these calculations by testing macroscale arrays of Au−Pd hetero-oligomers at both high (100%) and low (2%) hydrogen concentrations. These substrates showed a fast response time (seconds) and excellent sensor recovery. We anticipate that hetero-oligomers consisting of both strong plasmonic materials and reactant-specific elements will open a unique platform for optimizing plasmon-enhanced applications.

METHODS

Phase-Shifting Photolithography. A poly(dimethylsiloxane) (PDMS) stamp with line spacing a_0 = 400 nm was placed into conformal contact with diluted, positive-tone, g-line photoresist (PR) (Shipley S1805; ~120 nm thick) on a Si(100) wafer and exposed under a home-built solid-state photolithography system (emission at 405 nm with fwhm 10 nm). The mask was exposed twice (offset 90°) for 0.8 s to create square patterns. The exposed PR was developed in a 1:5 dilution of Microposit 351 developer and formed square arrays of PR posts on a Si substrate.

Finite Difference Time Domain Simulations. FDTD calculations based on commercial software (FDTD Solution, Lumerical Inc., Vancouver, Canada) were used to simulate the linear properties (far-field and near-field) of Au oligomers as well as the hydrogen-sensing performance of Au−Pd hetero-oligomers. The optical constants of Au were taken from Johnson and Christy[47] (400−1200 nm), and those of Pd and PdH_x were taken from ref 44 (400−1200 nm). The lattice expansion of Pd upon hydrogen injection was assumed to be 4% according to the literature.[43] (1) In simulations of Au oligomers, a uniform mesh size of 4 nm (x, y, and z directions) was used. The size of Au NPs was 120 nm × 60 nm × 30 nm. The center gap size was 35 nm, and the side gap size was 10 nm. (2) In simulations of Au−Pd oligomers, a uniform mesh size of 2 nm (x, y, and z directions) and another 0.5 nm mesh at the gap region were used to improve the spatial resolution of the field distribution. The size of Au and Pd NPs was 120 nm × 60 nm × 30 nm. The gap size of a Au−Pd dimer was 10 nm. The center gap size of a Au−Pd trimer was fixed at 25 nm, and the side gap size was varied from 11 to 0 nm.

Optical Measurements and High-Resolution Localized Surface Plasmon Resonance (HR-LSPR) Spectroscopy. The transmission spectra of Au oligomers were collected by a PerkinElmer Lambda 1050 UV/vis/NIR spectrophotometer, which is a high-performance UV/vis/NIR double-beam, double-monochromator, ratio-recording spectrophotometer. A high-resolution LSPR setup was used for H_2 gas sensing. Our HR-LSPR apparatus includes mass flow controllers to regulate flow rates and solenoid valves for precise switching between H_2 and N_2 gases. The samples were placed in a gas flow cell, and extinction spectra were collected with a resolution of 0.015 nm by HR-LSPR spectroscopy.[13,45] White light from a tungsten halogen lamp was focused to a ~1 mm diameter spot on the sample, and the transmitted light was refocused into a linear photodiode array spectrometer. A LabVIEW program was used to control gas dosing and to analyze the spectral shifts in real time by monitoring precisely the position of a selected peak over time.[43] This program automated analysis by acquiring spectra at 100 ms intervals, calculating the maximum wavelength by fitting a 100 nm spectral region around the peak to a fourth-order polynomial and displaying λ_{max} in real time.

Conflict of Interest: The authors declare no competing financial interest.

Acknowledgment. This work was supported primarily by the National Science Foundation (NSF) under NSF Award Numbers DMR-1121262 (A.Y., T.W.O., M.F.C., R.V.D.). We also acknowledge support from NSF Award Number CHE-105801 (T.W.O.). This work made use of the EPIC facility (NUANCE Center, Northwestern University), which has received support from the MRSEC program (NSF DMR-1121262) at the Materials Research Center, and the Nanoscale Science and Engineering Center (EEC-0118025/003), both programs of the National Science Foundation, the State of Illinois, and Northwestern University. This research was supported in part through the computational resources and staff contributions provided for the Quest high-performance computing facility at Northwestern University, which is jointly supported by the Office of the Provost, the Office for Research, and Northwestern University Information Technology.

Supporting Information Available: SEM images showing tunability of RML; simulations on Au oligomers and Au−Pd trimer arrays; performance of Au−Pd oligomers under low-concentration H_2. This material is available free of charge *via* the Internet at http://pubs.acs.org.

REFERENCES AND NOTES

1. Novotny, L.; van Hulst, N. Antennas for Light. *Nat. Photonics* **2011**, *5*, 83–90.
2. Kauranen, M.; Zayats, A. V. Nonlinear Plasmonics. *Nat. Photonics* **2012**, *6*, 737–748.
3. Berini, P.; De Leon, I. Surface Plasmon-Polariton Amplifier and Laser. *Nat. Photonics* **2011**, *6*, 16–24.
4. Kelly, K. L.; Coronado, E.; Zhao, L. L.; Schatz, G. C. The Optical Properties of Metal Nanoparticles: The Influence of

Size, Shape, and Dielectric Environment. *J. Phys. Chem. B* **2003**, *107*, 668–677.

5. Atay, T.; Song, J.-H.; Nurmikko, A. V. Strongly Interacting Plasmon Nanoparticle Pairs: From Dipole−Dipole Interaction to Conductively Coupled Regime. *Nano Lett.* **2004**, *4*, 1627–1631.
6. Jensen, T.; Kelly, L.; Lazarides, A.; Schatz, G. C. Electrodynamics of Noble Metal Nanoparticles and Nanoparticle Clusters. *J. Cluster Sci.* **1999**, *10*, 295–317.
7. Zhang, Z.; Weber-Bargioni, A.; Wu, S. W.; Dhuey, S.; Cabrini, S.; Schuck, P. J. Manipulating Nanoscale Light Fields with the Asymmetric Bowtie Nano-Colorsorter. *Nano Lett.* **2009**, *9*, 4505–4509.
8. Gómez, D. E.; Teo, Z. Q.; Altissimo, M.; Davis, T. J.; Earl, S. The Dark Side of Plasmonics. *Nano Lett.* **2013**, *13*, 3722–3728.
9. Fan, J. A.; Wu, C.; Bao, K.; Bao, J.; Bardhan, R.; Halas, N. J.; Manoharan, V. N.; Nordlander, P.; Shvets, G.; Capasso, F. Self-Assembled Plasmonic Nanoparticle Clusters. *Science* **2010**, *328*, 1135–1138.
10. Panaro, S.; Nazir, A.; Liberale, C.; Das, G.; Wang, H.; De Angelis, F.; Proietti Zaccaria, R.; Di Fabrizio, E.; Toma, A. Dark to Bright Mode Conversion on Dipolar Nanoantennas: A Symmetry-Breaking Approach. *ACS Photonics* **2014**, *1*, 310–314.
11. Biagioni, P.; Huang, J.; Duò, L.; Finazzi, M.; Hecht, B. Cross Resonant Optical Antenna. *Phys. Rev. Lett.* **2009**, *102*, p256801.
12. Hatab, N. A.; Hsueh, C.-H.; Gaddis, A. L.; Retterer, S. T.; Li, J.-H.; Eres, G.; Zhang, Z.; Gu, B. Free-Standing Optical Gold Bowtie Nanoantenna with Variable Gap Size for Enhanced Raman Spectroscopy. *Nano Lett.* **2010**, *10*, 4952–4955.
13. Bingham, J. M.; Anker, J. N.; Kreno, L. E.; Van Duyne, R. P. Gas Sensing with High-Resolution Localized Surface Plasmon Resonance Spectroscopy. *J. Am. Chem. Soc.* **2010**, *132*, 17358–17359.
14. Sheikholeslami, S.; Jun, Y.; Jain, P. K.; Alivisatos, A. P. Coupling of Optical Resonances in a Compositionally Asymmetric Plasmonic Nanoparticle Dimer. *Nano Lett.* **2010**, *10*, 2655–2660.
15. Osberg, K. D.; Schmucker, A. L.; Senesi, A. J.; Mirkin, C. A. One-Dimensional Nanorod Arrays: Independent Control of Composition, Length, and Interparticle Spacing with Nanometer Precision. *Nano Lett.* **2011**, *11*, 820–824.
16. Liu, N.; Tang, M. L.; Hentschel, M.; Giessen, H.; Alivisatos, A. P. Nanoantenna-Enhanced Gas Sensing in a Single Tailored Nanofocus. *Nat. Mater.* **2011**, *10*, 631–636.
17. Shegai, T.; Johansson, P.; Langhammer, C.; Käll, M. Directional Scattering and Hydrogen Sensing by Bimetallic Pd−Au Nanoantennas. *Nano Lett.* **2012**, *12*, 2464–2469.
18. Tang, M. L.; Liu, N.; Dionne, J. A.; Alivisatos, A. P. Observations of Shape-Dependent Hydrogen Uptake Trajectories from Single Nanocrystals. *J. Am. Chem. Soc.* **2011**, *133*, 13220–13223.
19. Mirkin, C. A. Programming the Assembly of Two- and Three-Dimensional Architectures with DNA and Nanoscale Inorganic Building Blocks. *Inorg. Chem.* **2000**, *39*, 2258–2272.
20. Barrow, S. J.; Wei, X.; Baldauf, J. S.; Funston, A. M.; Mulvaney, P. The Surface Plasmon Modes of Self-Assembled Gold Nanocrystals. *Nat. Commun.* **2012**, *3*, 1275–1283.
21. Urban, A. S.; Shen, X.; Wang, Y.; Large, N.; Wang, H.; Knight, M. W.; Nordlander, P.; Chen, H.; Halas, N. J. Three-Dimensional Plasmonic Nanoclusters. *Nano Lett.* **2013**, *13*, 4399–4403.
22. Park, S. Y.; Lytton-Jean, A. K. R.; Lee, B.; Weigand, S.; Schatz, G. C.; Mirkin, C. A. DNA-Programmable Nanoparticle Crystallization. *Nature* **2008**, *451*, 553–556.
23. Gandra, N.; Abbas, A.; Tian, L.; Singamaneni, S. Plasmonic Planet−Satellite Analogues: Hierarchical Self-Assembly of Gold Nanostructures. *Nano Lett.* **2012**, *12*, 2645–2651.
24. Barrow, S. J.; Funston, A. M.; Gómez, D. E.; Davis, T. J.; Mulvaney, P. Surface Plasmon Resonances in Strongly Coupled Gold Nanosphere Chains from Monomer to Hexamer. *Nano Lett.* **2011**, *11*, 4180–4187.
25. Hentschel, M.; Saliba, M.; Vogelgesang, R.; Giessen, H.; Alivisatos, A. P.; Liu, N. Transition from Isolated to Collective Modes in Plasmonic Oligomers. *Nano Lett.* **2010**, *10*, 2721–2726.
26. Tang, Z.; Wei, A. Fabrication of Anisotropic Metal Nanostructures Using Innovations in Template-Assisted Lithography. *ACS Nano* **2012**, *6*, 998–1003.
27. Zhao, J.; Frank, B.; Burger, S.; Giessen, H. Large-Area High-Quality Plasmonic Oligomers Fabricated by Angle-Controlled Colloidal Nanolithography. *ACS Nano* **2011**, *5*, 9009–9016.
28. Syrenova, S.; Wadell, C.; Langhammer, C. Shrinking-Hole Colloidal Lithography: Self-Aligned Nanofabrication of Complex Plasmonic Nanoantennas. *Nano Lett.* **2014**, *14*, 2655–2663.
29. Qin, L. D.; Park, S.; Huang, L.; Mirkin, C. A. On-Wire Lithography. *Science* **2005**, *309*, 113–115.
30. Qin, L.; Jang, J.-W.; Huang, L.; Mirkin, C. A. Sub-5-nm Gaps Prepared by on-Wire Lithography: Correlating Gap Size with Electrical Transport. *Small* **2007**, *3*, 86–90.
31. Hulteen, J. C.; Van Duyne, R. P. Nanosphere Lithography: A Materials General Fabrication Process for Periodic Particle Array Surfaces. *J. Vac. Sci. Technol. A* **1995**, *13*, 1553–1558.
32. Rogers, J. A.; Paul, K. E.; Jackman, R. J.; Whitesides, G. M. Using an Elastomeric Phase Mask for Sub-100 nm Photolithography in the Optical near Field. *Appl. Phys. Lett.* **1997**, *70*, p2658.
33. Huntington, M. D.; Odom, T. W. A Portable, Benchtop Photolithography System Based on a Solid-State Light Source. *Small* **2011**, *7*, 3144–3147.
34. Nagpal, P.; Lindquist, N. C.; Oh, S. H.; Norris, D. J. Ultrasmooth Patterned Metals for Plasmonics and Metamaterials. *Science* **2009**, *325*, 594–597.
35. Suh, J. Y.; Huntington, M. D.; Kim, C. H.; Zhou, W.; Wasielewski, M. R.; Odom, T. W. Extraordinary Nonlinear Absorption in 3d Bowtie Nanoantennas. *Nano Lett.* **2012**, *12*, 269–274.
36. Prodan, E. A Hybridization Model for the Plasmon Response of Complex Nanostructures. *Science* **2003**, *302*, 419–422.
37. Fan, J. A.; He, Y.; Bao, K.; Wu, C.; Bao, J.; Schade, N. B.; Manoharan, V. N.; Shvets, G.; Nordlander, P.; Liu, D. R.; *et al.* DNA-Enabled Self-Assembly of Plasmonic Nanoclusters. *Nano Lett.* **2011**, *11*, 4859–4864.
38. Tittl, A.; Yin, X.; Giessen, H.; Tian, X.-D.; Tian, Z.-Q.; Kremers, C.; Chigrin, D. N.; Liu, N. Plasmonic Smart Dust for Probing Local Chemical Reactions. *Nano Lett.* **2013**, *13*, 1816–1821.
39. Hubert, T.; Boon-Brett, L.; Black, G.; Banach, U. Hydrogen Sensors-a Review. *Sens. Actuators, B* **2011**, *157*, 329–352.
40. Tittl, A.; Kremers, C.; Dorfmüller, J.; Chigrin, D. N.; Giessen, H. Spectral Shifts in Optical Nanoantenna-Enhanced Hydrogen Sensors. *Opt. Mater. Express* **2011**, *2*, 111–118.
41. Kishore, S.; Nelson, J. A.; Adair, J. H.; Eklund, P. C. Hydrogen Storage in Spherical and Platelet Palladium Nanoparticles. *J. Alloys Compd.* **2005**, *389*, 234–242.
42. Vargas, W. E.; Rojas, I.; Azofeifa, D. E.; Clark, N. Optical and Electrical Properties of Hydrided Palladium Thin Films Studied by an Inversion Approach from Transmittance Measurements. *Thin Solid Films* **2006**, *496*, 189–196.
43. Flanagan, T. B.; Oates, W. A. The Palladium-Hydrogen System. *Annu. Rev. Mater. Sci.* **1991**, *21*, 269–304.
44. von Rottkay, K.; Rubin, M.; Duine, P. A. Refractive Index Changes of Pd-Coated Magnesium Lanthanide Switchable Mirrors upon Hydrogen Insertion. *J. Appl. Phys.* **1999**, *85*, 408–413.
45. Kreno, L. E.; Hupp, J. T.; Van Duyne, R. P. Metal−Organic Framework Thin Film for Enhanced Localized Surface Plasmon Resonance Gas Sensing. *Anal. Chem.* **2010**, *82*, 8042–8046.
46. Langhammer, C.; Larsson, E. M.; Kasemo, B.; Zorić, I. Indirect Nanoplasmonic Sensing: Ultrasensitive Experimental Platform for Nanomaterials Science and Optical Nanocalorimetry. *Nano Lett.* **2010**, *10*, 3529–3538.
47. Johnson, P. B.; Christy, R. W. Optical Constants of the Noble Metals. *Phys. Rev. B* **1972**, *6*, 4370.